Slope Traversal Controls for Planetary Exploration Rover on Sandy Terrain

Genya Ishigami
Department of Mechanical Engineering
Massachusetts Institute of Technology
77 Massachusetts Ave., Cambridge, MA, 02139, USA
ishigami@mit.edu

Keiji Nagatani
Department of Aerospace Engineering
Tohoku University
Aoba 6-6-01, Sendai, 980-8579, JAPAN
keiji@ieee.org

Kazuya Yoshida
Department of Aerospace Engineering
Tohoku University
Aoba 6-6-01, Sendai, 980-8579, JAPAN
yoshida@astro.mech.tohoku.ac.jp

Abstract

In this paper, two control approaches are presented for exploration rovers traversing sandy-sloped terrain. One of the proposed controls is a model-based feed-forward control using a characteristic diagram, called a *Thrust-cornering characteristic diagram*. It consists of various characteristic curves of wheel forces for varied wheel slip conditions. An appropriate steering maneuver for slope traversal can be found using the diagram with slope traversal criteria. The other control is a sensor-based feedback control. A key approach to this feedback control is to compensate for three types of slip, namely, the vehicle sideslip and longitudinal/lateral slips of a wheel. The feedback control calculates both steering and driving maneuvers that can compensate for these slips and also allow the rover to successfully traverse a sandy slope. The performances of these two control approaches are confirmed in slope traversal experiments using a four-wheeled rover test bed. The proposed controls are verified by quantitative evaluations of distance and orientation errors. Through the experiment, it was found that the two controls have advantages and disadvantages, and the possibility of merging the model-based control and the sensor-based control is discussed.

1 Introduction

Exploration rovers are required to traverse challenging terrain, such as crater hills or slopes on their target bodies to fulfill scientific missions. Loose sandy soil generally present in crater surfaces impedes the progress of a rover, making it difficult to traverse, enter, and crawl out

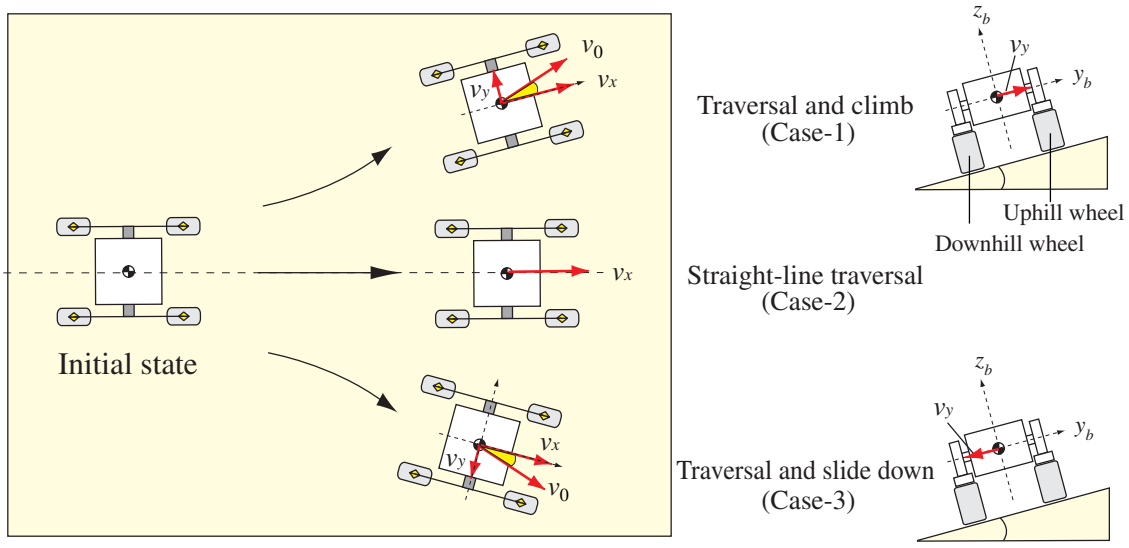

Figure 1: Slope traversal illustrations

of a crater because the wheels easily slip and get stuck on such terrain. In addition, the vehicle body of the rover experiences sideslip behavior due to the dynamic slips generated between wheels and terrain interfaces. As demonstrated by NASA/JPL Mars Exploration Rovers, the wheel slippage was particular concern when the rover traveled on sandy terrain (Maimone et al., 2007). Therefore, it is important to find an appropriate control strategy for the safe slope traversal of a rover.

When a rover traverses a side slope, as illustrated in Figure 1, the motion of the rover can be divided into three cases: Case-1, traversal and climb with positive lateral velocity of the vehicle; Case-2, straight-line traversal with zero lateral velocity; and Case-3, traversal and slide down with negative lateral velocity. From the figure, it may be deduced that a slope traversal, such as those in Case-1 and Case-3, can be achieved with sufficiently large (small) steering angles so that the rover may climb up (or slide down) a slope with the desired heading angle. In addition, the rover can traverse along a straight line on a slope with appropriate sets of steering angles, as in Case-2. Therefore, rovers need to execute their steering/driving maneuvers to achieve a required slope traversal task and to manage any slippage problems.

In this paper, two slope traversal controls to cope with slippage issues while slope traversing are proposed. The two control approaches are as follows: model-based feed-forward control and sensor-based feedback control.

Model-based feed-forward control: This control focuses on the force characteristics in terms of the wheel and vehicle. An appropriate counter-steering motion is required for desired slope traversal to generate a certain amount of wheel traction in comparison to the load of a vehicle parallel to the downhill direction due to gravity. The authors have developed a three-axis force model for a rigid wheel on loose terrain based on terramechanics (Ishigami et al., 2007). Furthermore, the authors have elaborated on an analytical diagram called a

thrust-cornering characteristic diagram by applying our wheel model to the analysis of the slope traversability of the rover (Ishigami et al., 2008b). This diagram determines the slope traversal criteria based on wheel slip conditions. In this model-based feed-forward control, steering maneuvers for slope traversal are obtained using a diagram with the traversability criteria.

Sensor-based feedback control: This control allows the rover to maneuver while successively correcting distance and heading errors according to a reference path. Sensors mounted on the rover, such as a visual odometry system, gyro, and inclinometer, measure these errors. A key approach of this feedback control is to compensate for three types of slips occurring on sandy terrain, namely, vehicle sideslip and longitudinal and lateral wheel slippages. The authors developed a method for distributing control tasks to the front and rear wheels to achieve slope traversal and slippage compensation. Subsequently, nonholonomic constraints of the vehicle properly include the vehicle sideslip and wheel lateral slip. Furthermore, the wheel longitudinal slip is addressed by controlling the wheel angular velocity. Based on this strategy, both steering and driving maneuvers of the rover can be derived to compensate for slippage and to allow the rover to traverse a sandy slope.

Slope traversal experiments using a four-wheeled rover test bed are conducted to confirm the usefulness of these two controls for the practical application. The rover test bed independently steers and drives its four wheels. For the accurate measurement of position, orientation, velocity, and slippage, the rover mounts a visual odometry system that is sufficiently robust for loose sandy terrain. The effectiveness of the proposed controls is verified by quantitative evaluations of distance and heading errors. In addition, we discuss the advantages and disadvantages of the two control schemes and describe the further enhancement of the slope traversal control.

This paper is organized as follows: Section 2 is a description of research related to this study, including path-following controls, terramechanics for wheel-vehicle dynamics, and measurement techniques for vehicle position, velocity, and slippage. In this section, the proposed controls are distinguished from those presented in related works. In Section 3, the model-based feed-forward control is addressed. The thrust-cornering characteristic diagram is introduced, and then, the derivation of steering maneuvers using the diagram is explained. The experimental validation of the feed-forward control is presented in Section 4. The sensor-based feedback control is described in Section 5 and the compensation for the three types of slippage is clarified. Steering and driving maneuvers are formulated along with nonholonomic/kinematic models of the vehicle. In Section 6, the slope traversal experiments using the feedback control are described, and the performance of the proposed approach is evaluated.

2 Related Works

In this section, a survey of the literature on path-following control, terramechanics for wheel dynamics on rough terrain, and measurement techniques for vehicle position and velocity is presented.

2.1 Path-Following Control

Significant studies on the topic of path-following tasks on rough terrain have been conducted. A general discussion regarding path-following issues can be found in (Luca et al., 1998; Rio et al., 1999; Wit et al., 1994). An on-line path-following strategy combined with a SLAM algorithm for a car-like robot in outdoor environments has been developed by (Rezaei et al., 2003). A Kalman-based active observer controller for the path following of wheeled mobile robots has been proposed by (Coelho and Nunes, 2005). (Helmick et al., 2004; Helmick et al., 2006) developed a path-following algorithm with slip compensation based on fusing visual odometry and inertial measurements through a Kalman filter.

These studies, however, do not specifically include wheel slippage in their feedback control systems. Our study in this paper is the first to thoroughly consider all vehicle and wheel slippage using the sensor-based feedback control and to include a validation of the usefulness of the control through an experiment. In addition, little research has been done to analyze the characteristics of wheel forces on slope traversal situations, and none has been done to utilize the force characteristics for the slope traversal control. Therefore, the model-based feed-forward control is also clearly distinguished from any other prior studies.

2.2 Terramechanics for Wheel-Vehicle Dynamics

The model-based feed-forward control described in this paper considers the wheel force characteristics on loose soil. Wheel-soil interaction mechanics is included in the field of *Terramechanics*. In this field, the principle of wheel-soil interaction mechanics and the empirical models of the stress distributions beneath the wheel have been thoroughly investigated by (Bekker, 1960; Bekker, 1969; Wong, 2001). Recently, these terramechanics-based models have been successfully applied to the motion analysis of planetary rovers as seen in (Iagnemma and Dubowsky, 2004). A simulator considering terrain environments and terrain-vehicle interactions has been developed by (Jain et al., 2003). A multibody system simulation for the longitudinal slip of tires with respect to a tire-soil interaction was also demonstrated by (Gibbesch and Schäfer, 2005).

Despite intensive studies pertaining to the mechanics of wheel-soil interaction, most are focused on the longitudinal wheel traction force. However, we have developed a three-axis force model including the lateral force characteristics of a wheel on loose soil, which is indispensable in a discussion of the slope traversal analysis. The thrust-cornering characteristic diagram is obtained using a wheel force model developed in our previous study (Ishigami et al., 2007), and it is used for the model-based feed-forward control.

2.3 Measurement Technique for Vehicle Position/Velocity

An adequate localization technique is necessary to measure position and heading errors and vehicle/wheel slippage to develop the sensor-based feedback control. The well-known wheel encoder-based odometry cannot secure accuracy as the rover travels over sandy terrain since the wheel of the rover easily slips, and as a result, the encoder will incorrectly calculate the

distance traveled.

Several approaches have been proposed to measure positions and calculate slippage in mobile robots. For example, (Reina et al., 2006) developed sensors used to detect wheel slippage and sinkage that were incorporated with onboard sensor modalities to improve robot localization. Furthermore, (Ojeda et al., 2006) proposed a wheel slippage detection system based on motor current measurements. (Angelova et al., 2006; Angelova et al., 2007) described a pose prediction method using stereo imagery by learning from previous examples of traversing similar terrain and applied it to characterize terrain properties. (Lamon, 2005; Lamon, 2008) proposed a robust position tracking technique in rough terrain by fusing different types of sensory inputs, such as 3D-Odometry, inertial measurement unit (accelerometers, gyros) and visual odometry. For the robot localization and slip measurement in our experiment, we use visual odometry with a telecentric optical system allowing a robust visual tracking of image flows of the ground. Detailed descriptions of this system are reported in Section 6.

3 Model-based Feed-forward Control

The model-based feed-forward control is developed based on an analytical diagram called *Thrust-cornering characteristic diagram*. In this section, first, slope traversal criteria are addressed; then, the thrust-cornering characteristic diagram is introduced along with the wheel force model. Furthermore, the approach of the feed-forward control is described.

3.1 Slope Traversal Criteria and Force Equilibrium

3.1.1 Slope traversal criteria

Figure 2 is a schematic figure with a slope traversal case. Here, we assume that the rover is a 4-wheel-drive/4-wheel-steer vehicle. When a rover traverses a sandy slope, the wheel of the rover generates forces in both the longitudinal and lateral directions of the wheel. In addition, a lateral slip of the wheel can be observed. This slippage in the lateral direction of the wheel is measured by slip angle β. The definition of the slip angle is explained later. Because of the wheel lateral slip, the wheel generates lateral force, identified as side force F_y. It can be clearly seen that the traction force parallel to the uphill direction is composed of the summation from F_{c1} to F_{c4}, which are the cornering forces of wheels. The cornering force F_c is given as a function of drawbar pull F_x and side force F_y:

$$F_c = F_x \sin\beta + F_y \cos\beta \tag{1}$$

The force balance between the traction force and the downhill-slope force (the component of the vehicle weight parallel to the downhill direction) determines three typical cases on the slope traversal as already shown in Figure 1. One of the slope traversal criteria can then be defined as follows:

$$\left.\begin{array}{ll} F_{c1}+F_{c2}+F_{c3}+F_{c4} > W\sin\theta_s & \text{(Case-1: Traversal and climb)} \\ F_{c1}+F_{c2}+F_{c3}+F_{c4} = W\sin\theta_s & \text{(Case-2: Straight line traversal)} \\ F_{c1}+F_{c2}+F_{c3}+F_{c4} < W\sin\theta_s & \text{(Case-3: Traversal and slide down)} \end{array}\right\} \tag{2}$$

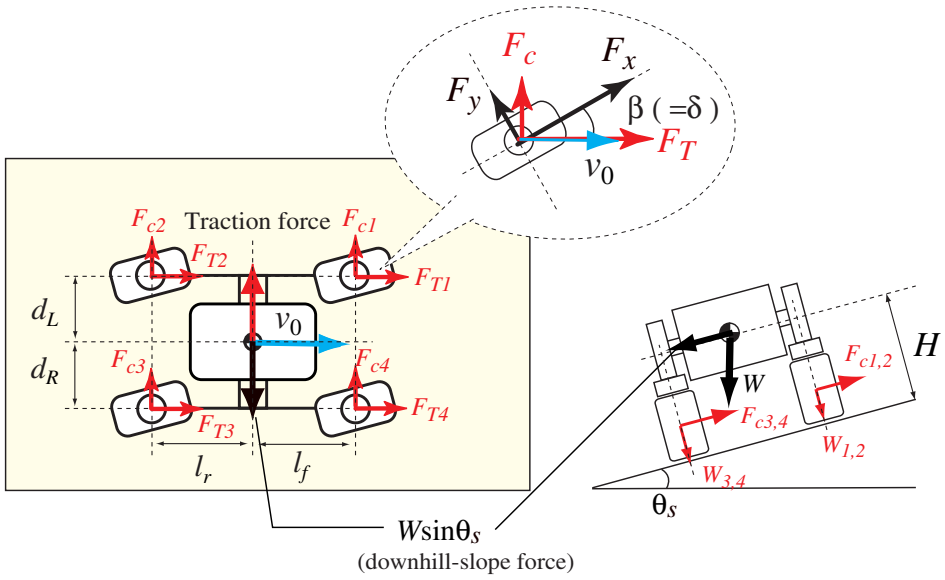

Figure 2: Force balance on slope traversal

where W is the vehicle weight, θ_s is the angle of inclination of the slope, and $W \sin\theta_s$ is the downhill-slope force.

Furthermore, with attention to the other force F_T, this resultant force F_T is defined as the thrust force and consists of a drawbar pull and side force:

$$F_T = F_x \cos\beta - F_y \sin\beta \tag{3}$$

The thrust force must be greater than zero so that the rover can travel the slope ahead. Then, the other slope traversal criterion is simply defined as:

$$F_{Ti} \geq 0 \quad (i = 1, \ldots, 4) \tag{4}$$

3.1.2 Force equilibrium point

When the rover traverses a slope along a straight line or with no-sideslip of the vehicle (this situation is illustrated in Case-2, Figure 1), a summation of the cornering forces is equal to the downhill-slope force as defined in Equation (2).

$$F_{c1} + F_{c2} + F_{c3} + F_{c4} = W \sin\theta_s \tag{5}$$

The above equation describes the force equilibrium of the vehicle on the slope in terms of uphill/downhill directions. Here, considering the force and moment balances between the vehicle and wheels, the required cornering force of each wheel for the straight-line traversal can be kinematically calculated as follows:

$$\left.\begin{aligned} F_{c1} &= \frac{W\sin\theta_s}{(1+l_f/l_r)\cdot(1+d'_L/d'_R)} \\ F_{c2} &= \frac{W\sin\theta_s}{(1+l_r/l_f)\cdot(1+d'_L/d'_R)} \\ F_{c3} &= \frac{W\sin\theta_s}{(1+l_r/l_f)\cdot(1+d'_R/d'_L)} \\ F_{c4} &= \frac{W\sin\theta_s}{(1+l_f/l_r)\cdot(1+d'_R/d'_L)} \end{aligned}\right\} \tag{6}$$

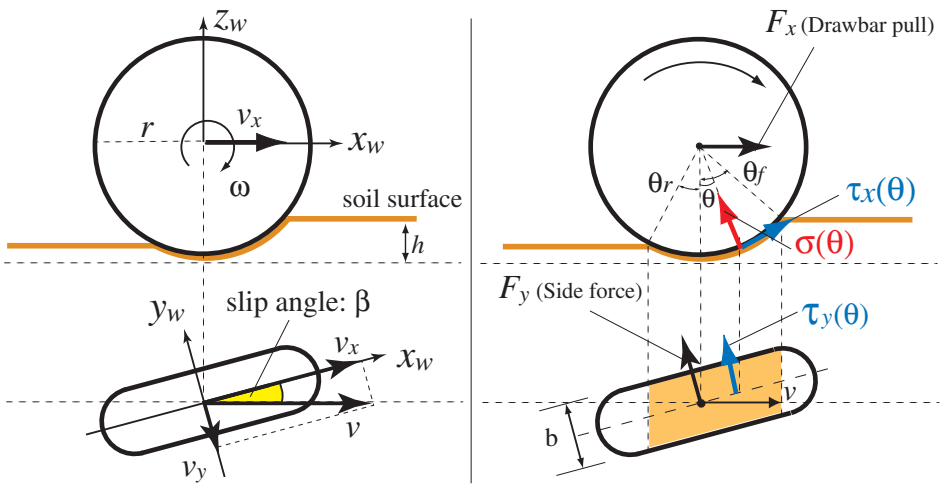

Figure 3: Analytical model of wheel force

where $d'_L = (d_L \cos\theta_s + H \sin\theta_s)$ and $d'_R = (d_R \cos\theta_s - H \sin\theta_s)$ are the horizontal components of the distance between the centroid of the vehicle and the centroid of the wheel, respectively; l_f and l_r represent the longitudinal distance from the centroid of the vehicle to the front or rear wheel; d_L and d_R define the lateral distance from the centroid of the vehicle to the left or right wheel; and H is the height of the centroid of the vehicle.

3.2 Definition of the Thrust-Cornering Characteristic Diagram

To develop the thrust-cornering characteristic diagram, an appropriate force model must be used to deal with the wheel force characteristics on loose sand because the slope traversal criteria defined as Equations (2) and (4) consist of the wheel forces.

Here, the wheel force model is briefly introduced on the basis of our previous work (Ishigami et al., 2007).

3.2.1 Force model for wheel on sandy terrain

As indicated in Equations (1) and (3), the characteristics of the thrust and cornering forces depend on the drawbar pull F_x, side force F_y, and slip angle β.

A general force model for a rigid wheel on loose soil is presented in Figure 3. Using the normal stress $\sigma(\theta)$ and the shear stress in the x direction $\tau_x(\theta)$, the drawbar pull F_x is calculated by the integral from the entry angle θ_f to the exit angle θ_r (Wong, 2001):

$$F_x = rb \int_{\theta_r}^{\theta_f} \{\tau_x(\theta) \cos\theta - \sigma(\theta) \sin\theta\} d\theta \tag{7}$$

where r is the wheel radius of wheel, and b is the width of the wheel.

The side force F_y is generated when the vehicle makes a steering maneuver. We have modeled

the side force as follows:

$$F_y = \int_{\theta_r}^{\theta_f} \{rb \cdot \tau_y(\theta) + R_b(h) \cdot (r - h(\theta)\cos\theta)\} d\theta \tag{8}$$

where $R_b(h)$ is the reaction resistance due to the bulldozing phenomenon on the side face of the wheel and is given as a function of wheel sinkage h. In addition, $\tau_y(\theta)$ is the shear stress in the y direction.

Note that $\sigma(\theta)$, $\tau_x(\theta)$, and $\tau_y(\theta)$, which are the key components to derive the wheel forces, are defined by the following equations:

$$\sigma(\theta) = \begin{cases} (ck_c + \rho b k_\phi)\left(\frac{r}{b}\right)^n [\cos\theta - \cos\theta_f]^n \\ \qquad (\theta_m \le \theta < \theta_f) \\ (ck_c + \rho b k_\phi)\left(\frac{r}{b}\right)^n \left[\cos\{\theta_f - \frac{\theta - \theta_r}{\theta_m - \theta_r}(\theta_f - \theta_m)\} - \cos\theta_f\right]^n \\ \qquad (\theta_r < \theta \le \theta_m) \end{cases} \tag{9}$$

$$\tau_x(\theta) = (c + \sigma(\theta)\tan\phi)[1 - e^{-j_x(\theta)/k_x}] \tag{10}$$

$$\tau_y(\theta) = (c + \sigma(\theta)\tan\phi)[1 - e^{-j_y(\theta)/k_y}] \tag{11}$$

where k_c and k_ϕ represent the pressure sinkage moduli; n is the sinkage exponent; θ_m is the maximum stress angle; c is the cohesion stress of soil; ϕ is the internal friction angle of soil; ρ is the density of soil; and j_x and j_y are the soil deformations. k_x and k_y are the soil deformation moduli describing the stiffness of the shear phenomenon at the interaction patch between the wheel surface and soil. We have assumed that the moduli can also represent the shear effect due to the wheel surface pattern, such as lugs, spikes, or grousers. Detailed descriptions and experimental validation of this model are found in (Ishigami et al., 2007).

Characteristics of both the drawbar pull and side force vary with wheel slippages. The wheel slippage is separated into longitudinal and lateral directions of wheel. The slip in the longitudinal direction is expressed by the slip ratio s, which is defined as a function of the longitudinal traveling velocity of the wheel v_x and the circumference velocity of the wheel $r\omega$ (ω represents the angular velocity of the wheel) (Wong, 2001):

$$s = \begin{cases} (r\omega - v_x)/r\omega & (|r\omega| > |v_x| : \text{driving}) \\ (r\omega - v_x)/v_x & (|r\omega| < |v_x| : \text{braking}) \end{cases} \tag{12}$$

The slip ratio assumes a value in the range from -1 to 1.

On the other hand, the slip in the lateral direction is expressed by the slip angle β, which is defined by v_x and the lateral traveling velocity v_y as follows:

$$\beta = \tan^{-1}(v_y/v_x) \tag{13}$$

3.2.2 Thrust-cornering characteristic diagram

Thrust and cornering forces with different slip ratios/slip angles can be obtained by calculating the drawbar pull and side force. Numerical procedures to calculate the thrust and cornering forces are as follows: first, input wheel load, slip ratio s, and slip angle β. Subsequently, calculate wheel sinkage h and wheel contact angles θ_f and θ_r. Finally, determine the

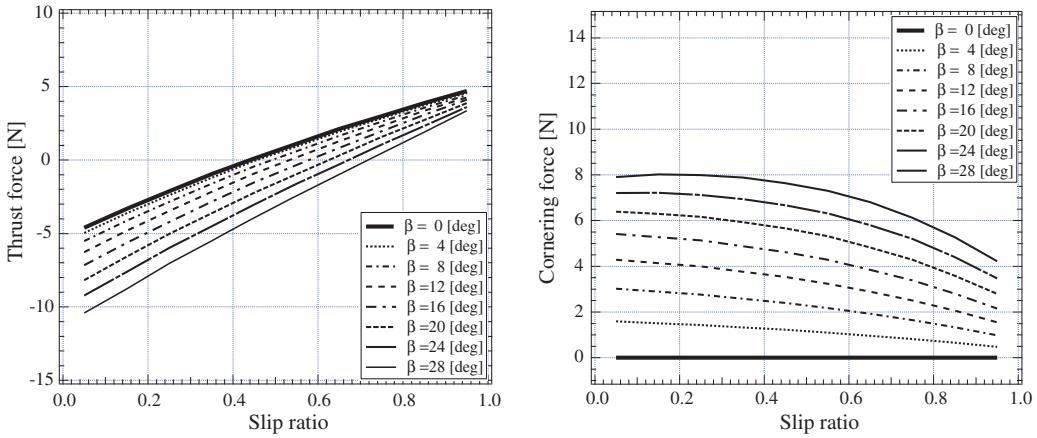

(a) : Thrust force (b) : Cornering force

Figure 4: Characteristic curves of thrust and cornering force

Table 1: Soil parameters and values

Parameter	Value	Unit	Description
c	0.0	[kPa]	Cohesion stress
ϕ	38.0	[deg]	Friction angle
k_c	0.0	[-]	Pressure-sinkage modulus
k_ϕ	1203.54	[-]	Pressure-sinkage modulus
ρ	1.49×10^3	[kg/m^3]	Soil density
n	1.703	[-]	Sinkage exponent
k_x	0.07	[m]	Shear deformation modulus
k_y	0.03	[m]	Shear deformation modulus
r	0.055	[m]	Wheel radius
b	0.064	[m]	Wheel width

drawbar pull and side force by Equations (7) and (8), and the thrust and cornering forces are then determined by Equations (3) and (1).

A typical example for characteristic curves of thrust and cornering forces with varied slip ratio/slip angles are shown in Figure 4. Soil parameters used to obtain these graphs are listed in Table 1. The wheel load is set as 29.8 [N]. The test soil in this simulation is assumed as Toyoura sand, which is used in the experiments described later. From the graph, the characteristics of these forces can be summarized as follows: the thrust force increases as the slip ratio increases, but it decreases as the slip angle increases. In addition, the cornering force decreases along with the slip ratio and increases according to the slip angle.

We then developed the following approach: combining the characteristic curves shown in Figure 4-(a) and (b), the relationship between the thrust and cornering forces with varied slip ratios/slip angles can be obtained as a diagram as shown in Figure 5.

This diagram has been proposed as the *Thrust-cornering characteristic diagram* (Ishigami et al., 2008b). The horizontal axis of the diagram is the thrust force, while the vertical axis is

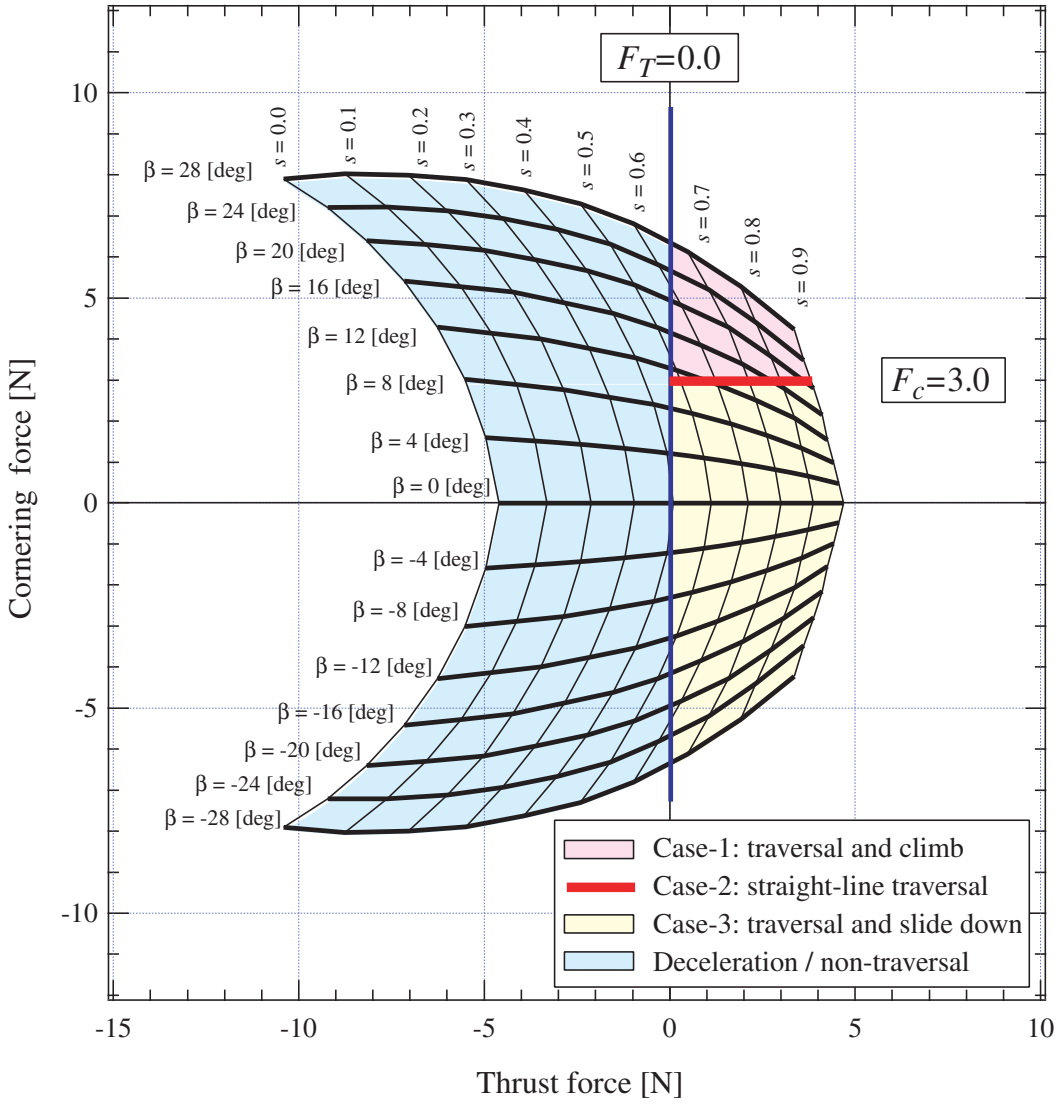

Figure 5: Thrust-cornering characteristic diagram

the cornering force. The upper half of this diagram is equivalent to the one for the front-left wheel as shown later in Figure 7-(a) at 5 [deg] of slope angle.

Here, for instance, the required cornering force F_c is assumed to be 3.0 [N]. In addition, referring to one of the slope traversal criteria determined in Equation (4), the required thrust force is given as $F_T \geq 0$. Subsequently, drawing these two criteria lines ($F_c = 3.0$, $F_T = 0$) on the diagram, the diagram describes the three typical slope traversal cases: the pink region ($F_c > 3.0$, $F_T \geq 0$) is noted as "Case-1 traversal and climb;" the red line ($F_c = 3.0$, $F_T \geq 0$) is "Case-2 straight-line traversal," and the yellow region ($F_c < 3.0$, $F_T \geq 0$) is "Case-3 traversal and slide down." In addition, a rover decelerates or can not move forward when wheel slippage occurs, which is indicated by the blue region in the 2nd and 3rd quadrants ($F_T < 0$).

In the example above, the slip ratio must exceed 0.6 in order to generate positive thrust force, and, in addition, the cornering force varies primarily with the slip angle. Therefore, the slope traversability of the rover is determined on the basis of the corresponding slippage, indicated by several characteristic curves on the diagram. In this diagram, if the wheel has roughly more than 12 [deg] of slip angle and 0.6 of slip ratio, the rover can traverse and climb the sloped terrain.

It is noteworthy that the diagram can be applied to any terrain (sandy, muddy, or hard) and any wheel dimensions once terrain parameters and wheel shapes are given to the wheel force model.

3.3 Approach of Model-based Feed-forward Control

At the force equilibrium point (Case-2, straight-line traversal), the wheel steering angle δ is equivalent to the wheel slip angle. Therefore, once the required cornering force for the straight-line traversal is given by Equation (6), the thrust-cornering characteristic diagram provides the corresponding slip angle (=steering angle) to generate the required cornering force as an intersection point at which the two criteria lines cross. As shown in Figure 5, a rover having between 8 [deg] and 12 [deg] of steering angles with a certain amount of slip ratio can achieve a straight-line traversal on the slope. In other words, a rover with more than (or less than) 12 [deg] of steering angles can traverse and climb (or slide down) a sloped terrain. Therefore, we can choose and provide three distinct traversal motions for the rover using the thrust-cornering characteristic diagram.

The procedure of the model-based feed-forward control is summarized as follows:

1. Derive the required cornering forces on an arbitrary angle of a slope with Equation (6).
2. Calculate the normal load of each wheel to the sloped terrain and then calculate a thrust-cornering characteristic diagram with respect to the wheel normal load.
3. Using the thrust-cornering characteristic diagram, draw the required F_c and $F_T = 0$.
4. Find the slip angle at which the two criteria lines intersect on the diagram.
5. Determine the steering angle δ with consideration of the three traversal cases.

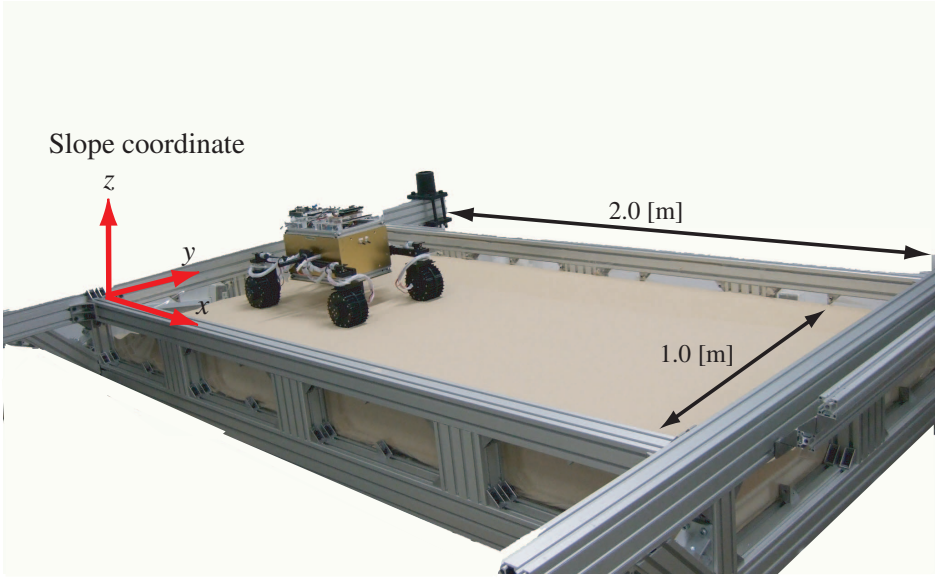

Figure 6: Overview of the experimental setup

6. Calculate the driving velocity ω_d (=wheel angular velocity) with the desired velocity v_d and steering angle as $\omega_d = v_d \cos\delta / r$.

The above procedures are conducted for all wheels of the rover to find the feed-forward steering angles of every wheel. In step 2, the normal load is calculated while considering the kinematics/dynamics parameters of the rover test bed, such as the mass and inertia of the components dimensions.

4 Slope Traversal Experiment with Model-based Feed-forward Control

Side-slope traversal experiments were carried out to confirm the usefulness of the model-based feed-forward control for practical applications.

4.1 Experimental Setup

Figure 6 is an overview of the experimental setup with the rover test bed. The test field, 2.0 [m] × 1.0 [m], consists of a rectangular tiltable vessel. The vessel is filled up with 8.0 [cm] depth of Toyoura Sand, which is cohesion-less loose sand and is also well-known as a standard in the field of terramechanics research (Toyoura Sand, 2008; Kobayashi et al., 2006). The four-wheeled test rover is 0.44 [m] (wheelbase) × 0.30 [m] (tread) × 0.30 [m] (height) and weighs about 13.5 [kg]. Each wheel of the rover with a radius of 5.5 [cm] and a width of 6.4 [cm] is covered with lugs with a heights of 0.5 [cm].

We employed a motion capture camera (Stereo Labeling Camera developed by CyVerse

Corp.), which can measure the corresponding positions of reflectors mounted on the rover. This stereo camera is fixed on a tripod stand so that the camera view is downward over the entire test field. The distance between the camera and the reflectors is 2.5 [m] and this setup enables the position measurement of the rover with a horizontal accuracy of 0.01 [m]. The velocity of the rover is calculated by the derivative of the time history of the position data. In addition, the vehicle orientation around the yaw axis (the heading of the rover) is calculated by a tangential angle obtained by the time-consecutive displacements of two different reflectors.

The experiments were conducted in two cases: in case-A, the slope angle was 5 [deg], and in case-B, it was 10 [deg]. On each slope angle, the initial heading of the rover was set along the x axis of the slope coordinate (= no initial heading error).

4.2 Derivation of Feed-forward Control Parameters

In the experiment, the rover is controlled to achieve a straight-line traversal. Based on the model-based feed-forward control described in Section 3, thrust-cornering characteristic diagrams are calculated as shown in Figures 7 and 8. We focus on the upper half of the diagram. The normal load and required cornering force for the straight-line traversal are summarized in Tables 2 and 3, respectively. The soil parameters used for the calculation of the diagram are shown in Table 1.

From the diagrams, the derived steering angles are around 7.0 [deg] for case-A, and around 20.0 [deg] for case-B. These derived steering angles are given as the initial steering angles of the rover, and steering motions during each test run are controlled to maintain the derived steering angles. The desired velocity v_d is set to 0.02 [m/s]. The wheel angular velocities ω_d are set as described in Section 3.3, along with the corresponding steering angles.

4.3 Experimental Results and Discussion

The experimental results regarding the slope traversal trajectory are shown in Figures 9 and 10. A certain number of the slope traversal runs were conducted and two typical experimental results in each case are shown in this paper. The errors for distance and orientation (heading) are summarized in Table 4. The distance error is given as the lateral deviation of the position from the straight line at the final state. The error percentage for the position is calculated by dividing the error value at the final state by the total travel distance, while that for the orientation is determined by dividing the error value by $\pi/2$.

From the figures for the slope traversal trajectories, it can be seen that the rover traversed and climbed the slope in each case with slight change of its heading. As summarized in the tables, position and orientation errors are within a few percentage points of one another. In case-B, we observed that the slip angle was around 23 [deg]. Because of this large slip angle compared to the derived steering angle (around 20 [deg]), the cornering forces of wheels were larger than the downhill-slope force, and the vehicle traversed and climbed the slope. In addition, the slip ratio was measured to be around 0.5. This value of the slip ratio was

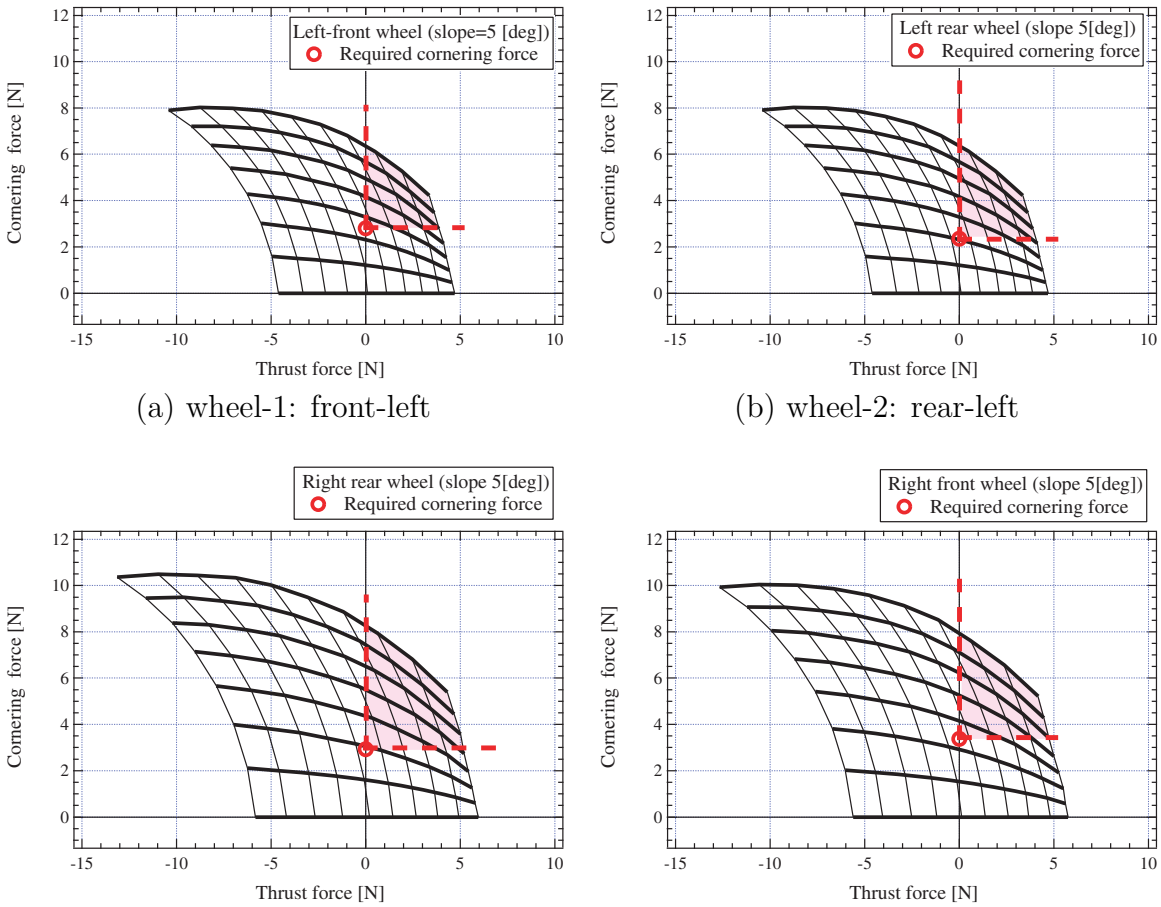

(a) wheel-1: front-left (b) wheel-2: rear-left

(c) wheel-3: rear-right (d) wheel-4: front-right

Figure 7: Thrust-cornering characteristic diagram: case-A (slope angle 5 [deg])

Table 2: Feed-forward control parameters: case-A (slope angle 5 [deg])

Wheel	1 (front-left)	2 (rear-left)	3 (rear-right)	4 (front-right)
Normal load [N]	29.8	29.8	37.1	35.9
Required cornering force [N]	2.8	2.4	2.9	3.4
Derived steering angle [deg]	6.7	7.0	7.0	6.7

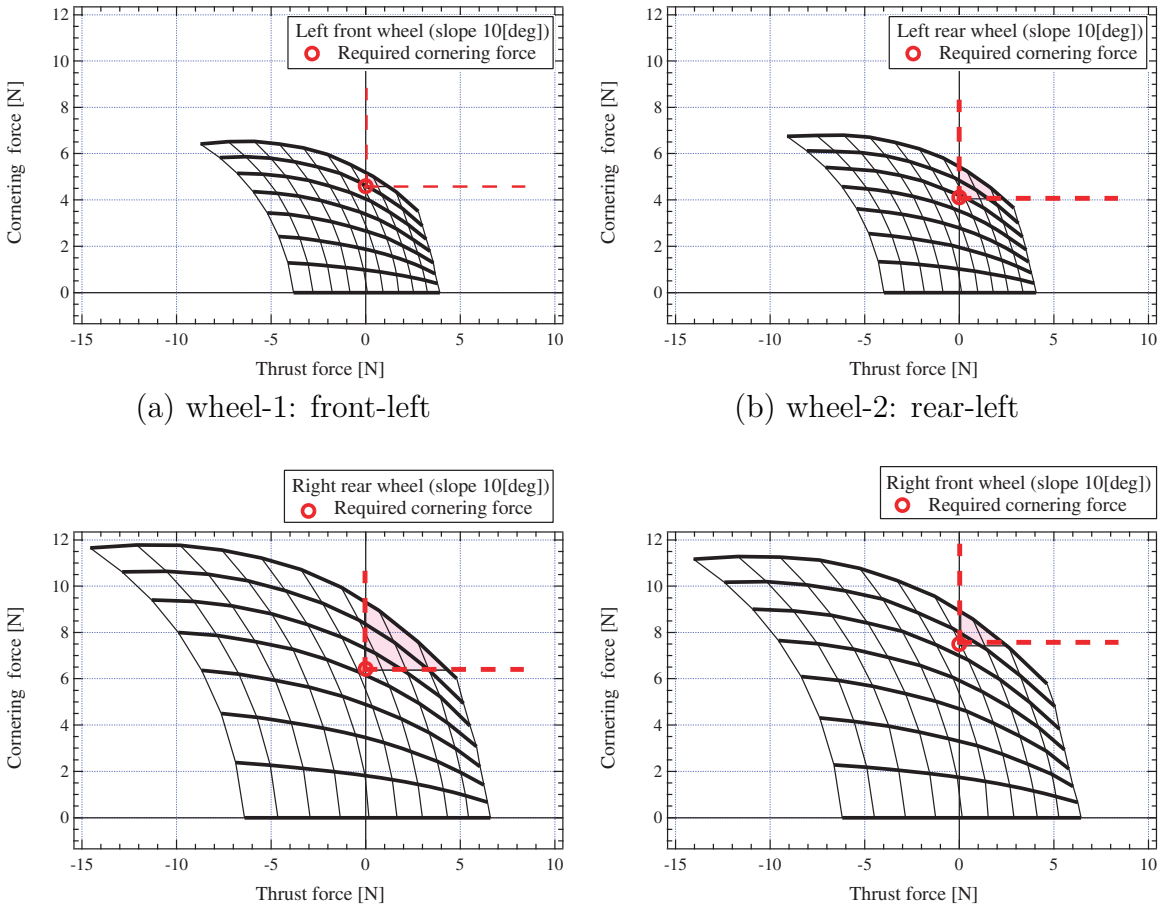

(a) wheel-1: front-left (b) wheel-2: rear-left

(c) wheel-3: rear-right (d) wheel-4: front-right

Figure 8: Thrust-cornering characteristic diagram: case-B (slope angle 10 [deg])

Table 3: Feed-forward control parameters: case-B (slope angle 10 [deg])

Wheel	1 (front-left)	2 (rear-left)	3 (rear-right)	4 (front-right)
Normal load [N]	25.3	26.1	41.0	39.4
Required cornering force [N]	4.8	4.1	6.4	7.5
Derived steering angle [deg]	18.9	19.5	19.5	18.9

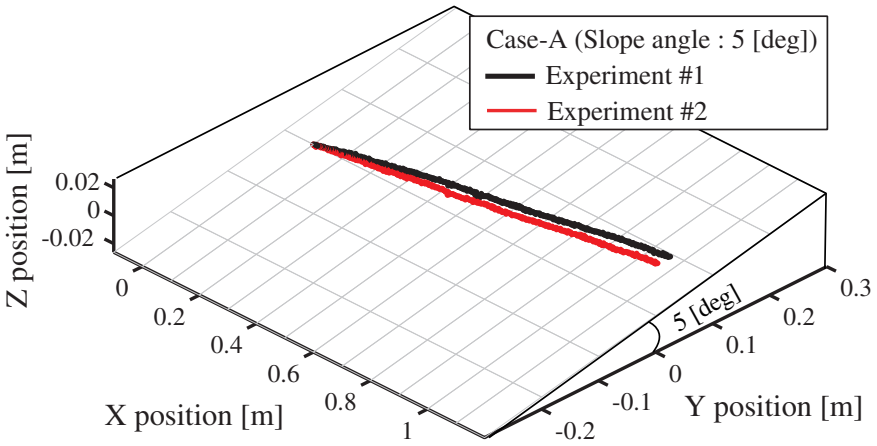

Figure 9: Slope traversal trajectory : case-A (slope angle 5 [deg])

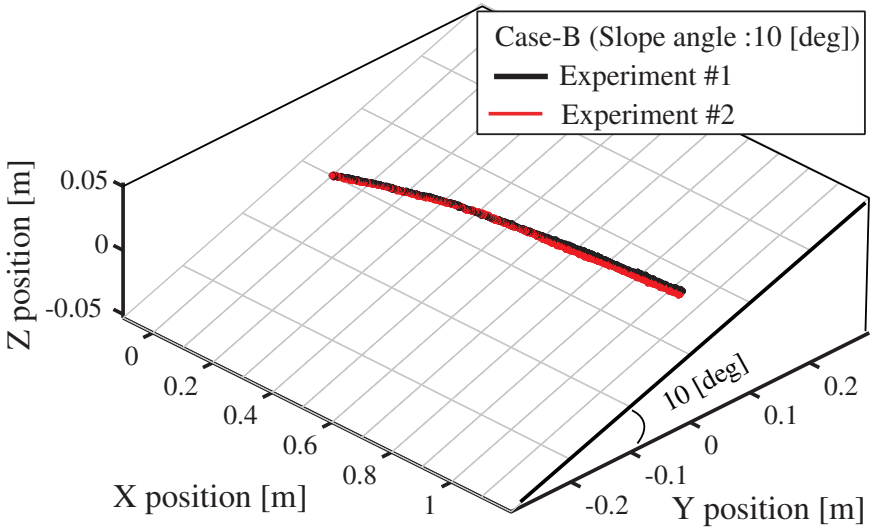

Figure 10: Slope traversal trajectory : case-B (slope angle 10 [deg])

Table 4: Slope traversal errors : model-based feed-forward control

Slope anlge [deg]		Orientation error [deg]		Distance error [m]	
		rms	Final state	rms	Final state
Case-A	5.0 (#1)	2.79 (3.09 %)	3.24 (3.60 %)	0.058 (5.42 %)	0.096 (9.04 %)
	(#2)	1.42 (1.58 %)	0.88 (0.97 %)	0.044 (4.21 %)	0.077 (7.31 %)
Case-B	10.0 (#1)	2.25 (2.50 %)	3.91 (4.34 %)	0.051 (4.98 %)	0.072 (6.99%)
	(#2)	1.31 (1.45 %)	0.59 (0.65 %)	0.049 (4.78 %)	0.069 (6.67%)
	Average	1.94 (2.16 %)	2.16 (2.39 %)	0.051 (4.59 %)	0.079 (7.50%)

predicted as the intersection of the two criteria lines on the diagrams.

It is deduced that the position/orientation errors are due to a mismatch of the soil parameters used in the wheel model; the wheel model described in Section 3 needs soil parameters to characterize the wheel forces. However, the real values of the soil covering the test field includes uncertainties and, in addition, do not completely agree with the values of the soil parameters used in the wheel force model. Because of this, the steering angles derived from the thrust-cornering characteristic diagrams were larger than appropriate steering angles that enable the straight-line traversal.

The accuracy of the wheel force model and the thrust-cornering characteristic diagram depend significantly on the accuracy of the measured soil parameters. Regarding the sensitivity analysis of the wheel model to soil parameters, based on a previous study by (Ishigami et al., 2007), a dynamics model including the wheel force model has shown good performance (roughly less than 10 %) to predict motion trajectory of the rover traveling on loose terrain. As described above, the model-based control using this wheel force model also shows less than 10 % of error in the slope traversal control. Therefore, it is clear that the model-based feed-forward control works well for slope traversal within the accuracy of the wheel force model. In a practical situation, this feed-forward control requires an *in-situ* estimation methods for soil parameters. Several studies have been presented a thorough discussion of soil parameter estimation methods e.g., (Iagnemma et al., 2002).

5 Sensor-based Feedback Control

As discussed in Section 4, the model-based feed-forward control enables the rover to traverse a slope, but this approach requires accurate prior information of the soil parameters, since the control performance is limited because of the uncertainty of the soil parameters. In addition, the feed-forward control needs to conduct an in-situ determination of soil parameters when a rover travels through unknown environments.

In this section, the sensor-based feedback control, which is independent of the terrain features and soil parameters, is discussed. The sensor-based feedback control allows a rover to successively correct distance and heading errors according to a reference path as well as to compensate for wheel and vehicle slippage.

First, an approach for the proposed control is introduced with a description of the problems of conventional approaches for path following in slipping environments. The derivation of both steering and driving maneuvers is also formulated using a nonholonomic kinematic model of the vehicle which takes slippage into account.

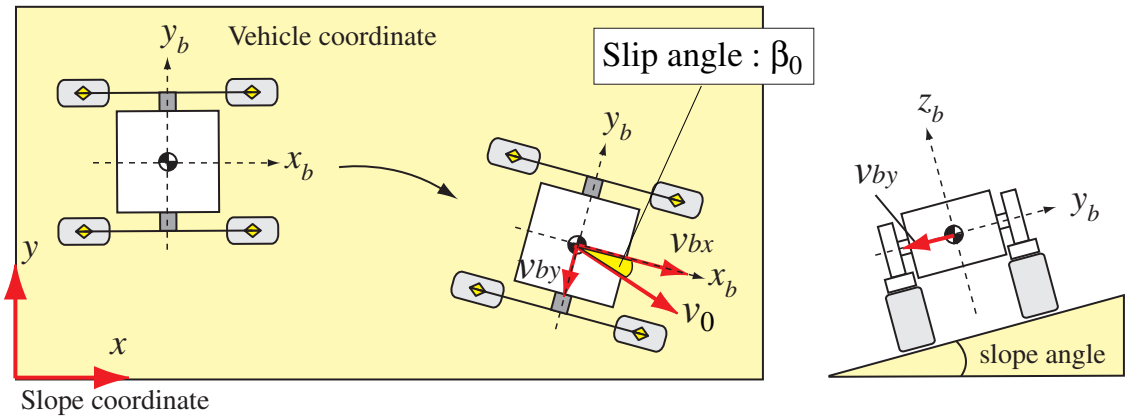

Figure 11: Definition of the slip angle of a vehicle

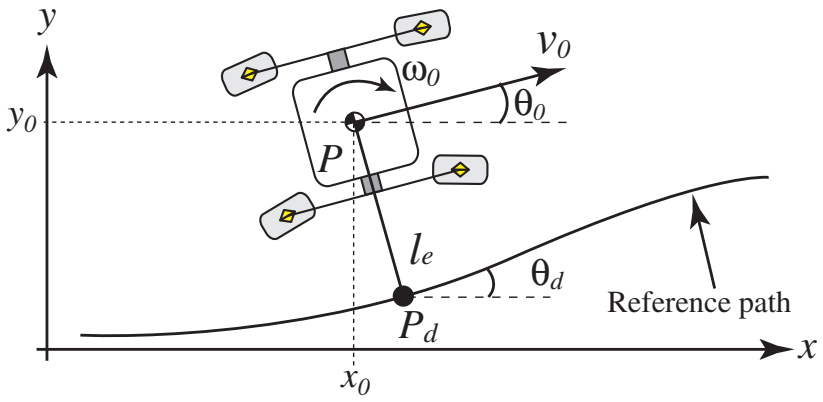

Figure 12: Illustration of path following (w/o sideslip)

5.1 Approach of Sensor-based Feedback Control

5.1.1 Problem statement

When a rover traverses a slope of loose sand, the vehicle body of the rover experiences a sideslip, which is measured by a slip angle. As shown in Figure 11, the slip angle of the vehicle, β_0, is calculated by using the longitudinal and lateral linear velocities on the vehicle coordinate, v_{bx} and v_{by}, as follows:

$$\beta_0 = \tan^{-1}(v_{by}/v_{bx}) \tag{14}$$

Based on the kinematics and terramechanics, a non-zero slip angle of the vehicle also occurs due to the cornering effect associated with the wheel slippage. The wheel slippage can be divided into longitudinal and lateral slips, as noted in Section 3. A key issue of the sensor-based feedback control is the compensation of these three slips, namely vehicle sideslip and wheel longitudinal/lateral slips, while the rover follows an arbitrary path.

A general illustration of the path-following problem is shown in Figure 12. In the path-

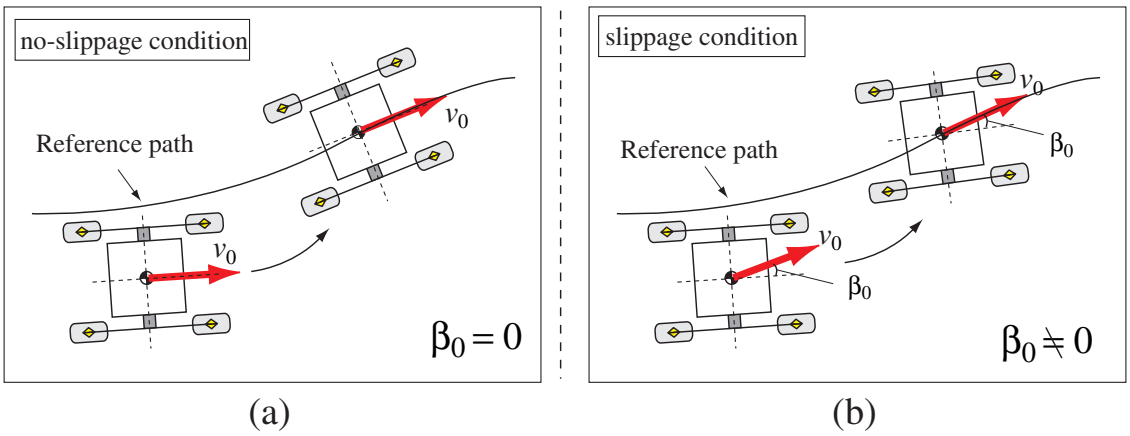

Figure 13: Path-following problem w/ and w/o slip angle of vehicle

following problem, a feedback control law is employed to reduce both distance and orientation errors. Here, θ_0 is the vehicle orientation around the yaw-axis of the vehicle; θ_d is the vehicle's desired orientation and it consists of the angle between the x axis of the inertial coordinate system and the tangent to the path at P_d; l_e is the distance error (distance between P and P_d); and θ_e is the orientation (heading) error, given as $\theta_0 - \theta_d$.

Referring to the conventional path-following algorithm in (Wit et al., 1994), a vehicle is controlled so that the vector of the vehicle velocity v_0 coincides with the tangent of a given path as shown in Figure 13-(a). The slip angle of the vehicle is assumed to be negligible in this case, and therefore, the conventional control has been verified in a no-slippage condition. However, as shown in Figure 13-(b), if the vehicle experiences a sideslip with a certain amount of slip angle β_0, this slip angle becomes an additional orientation error even when the vector of vehicle velocity follows the path. From the above statement, the orientation error for a path-following problem in a high-slippage environment needs to be considered as a combination of both pure orientation error θ_e and also slip angle β_0.

5.1.2 Sensor-based feedback control: Slip compensation control with path following

As noted above, a feedback control law works to satisfy both zero distance and zero orientation errors in order to follow a given path. In this research, we consider that the orientation error separately consists of two different angles, $\theta_e (= \theta_0 - \theta_d)$ and β_0. If the orientation error is assumed as a set of them, namely $\theta_e = \theta_0 - \theta_d + \beta_0$, the vehicle orientation cannot reach the desired orientation θ_d. Therefore, the control objectives in our proposed control can be defined as $l_e \rightarrow 0$, $\theta_e \rightarrow 0$, and $\beta_0 \rightarrow 0$. The first two objectives appear in a conventional path-following schemes, but the last one is relatively unique and becomes necessary only when the vehicle experiences a skidding (drifting) motion with sideslip (lateral slip) of the wheels.

In this research, we considered to apply the proposed control to a 4-wheel-drive/4-wheel-steer vehicle. To fulfill the slip compensation control while following a path follow, we developed

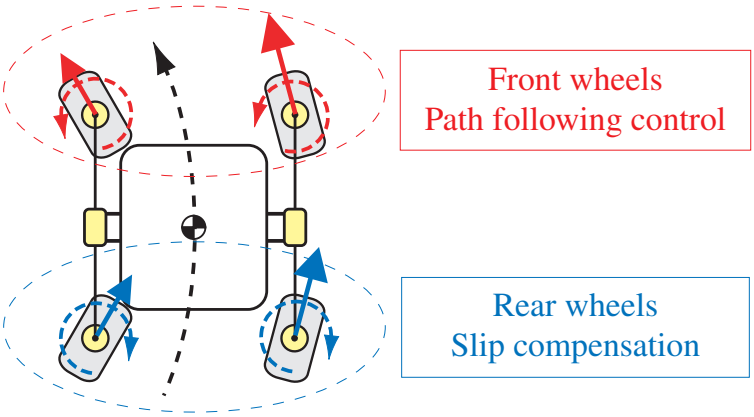

Figure 14: Approach of slip compensation control with path following

a method requiring the front pair of wheels to execute the conventional path following ($l_e \to 0$ and $\theta_e \to 0$), and the rear pair of them to compensate for the sideslip ($\beta_0 \to 0$), as illustrated in Figure 14. The distribution of path following and slip compensation into front/rear wheels is explained in the following. As evident in a conventional forklift, it is well known that rear-wheel steering enables a vehicle to increase maneuverability in tight cornering situations because the turning pivot is located ahead of the rear wheels. In addition, the front wheel maneuvers for path following occasionally generate additional vehicle sideslip around the turning pivot located at the centroid of the vehicle, but the rear-wheel pair works to cancel the sideslip by applying counter-steering motion in response to the front wheel around the pivot.

These control objectives are achieved by using one control variable, which is a turning angular velocity of vehicle $\dot{\theta}_d$. Considering a linear state feedback control when v_0 is not to be zero, the principle control law for the front pair is

$$\dot{\theta}_d = -k_1 v_0 l_e - k_2 |v_0| \theta_e - k_3 |v_0| \dot{\theta}_e \tag{15}$$

and that for the rear pair is:

$$\dot{\theta}_d = k_4 \beta_0 - k_5 |v_0| \theta_e - k_6 |v_0| \dot{\theta}_e \tag{16}$$

where $k_1, \ldots, k_6$ are control gains. These two control laws are executed by both steering and driving maneuvers as formulated in the following section.

5.2 Derivation of Steering and Driving Maneuvers

The slip compensation control with path following is practically accomplished by several actuators that are located on the steering and wheel driving axles. We have proposed a method to distribute the control inputs to both steering and driving axles while taking into account the wheel slippage, as described in (Ishigami et al., 2008a). In order to derive appropriate maneuvers, nonholonomic constraints of a four-wheeled vehicle including the vehicle's sideslip and the lateral slip of wheels are considered. In addition, controlling the wheel angular velocities of driving axles compensates for longitudinal wheel slippage.

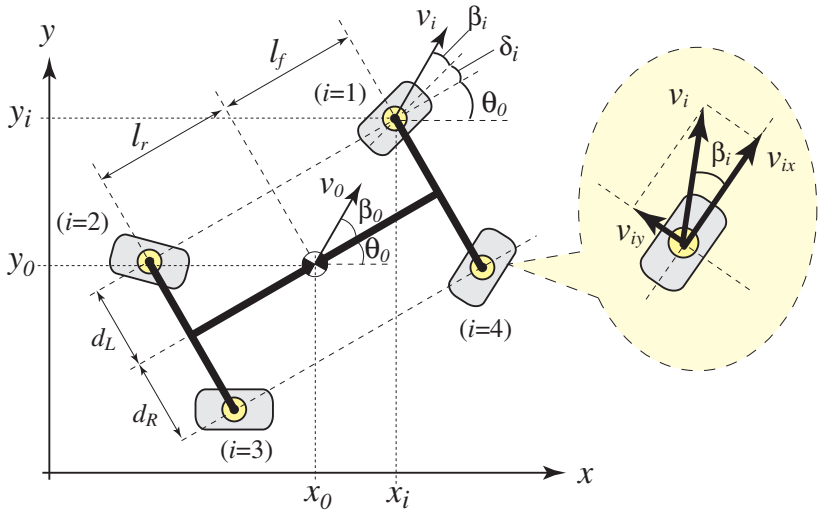

Figure 15: Kinematic model of four-wheeled vehicle

5.2.1 Nonholonomic kinematic model of vehicle

To discuss the nonholonomic kinematic model, the following assumptions are considered: 1) the distance between wheels (generally called wheelbase and tread) are strictly fixed and constant; 2) the steering axle of each wheel is perpendicular to the terrain surface; 3) the vehicle does not consist of any flexible parts.

A kinematic model of a four-wheeled vehicle including the slip angle of a vehicle and lateral wheel slippage is shown in Figure 15. In this model, each wheel has a steering angle δ_i and a slip angle of wheel β_i. The subscript i denotes the wheel ID ($i = 1, \ldots, 4$, in this case). The position and orientation of the centroid of the vehicle are defined as (x_0, y_0, θ_0), while (x_i, y_i) gives the position of each wheel. v_i is the linear velocity of each wheel. l_f and l_r represent the longitudinal distance from the centroid of the vehicle to the front or rear wheel and d_R and d_L define the lateral distance from the centroid of the vehicle to the left or right wheel, as already defined in Section 3.1.2.

The nonholonomic constraints are expressed by the following equation, taking into account the lateral slips:

$$\dot{x}_0 \sin\phi_0 - \dot{y}_0 \cos\phi_0 = 0 \tag{17}$$

$$\dot{x}_i \sin\phi_i - \dot{y}_i \cos\phi_i = 0 \tag{18}$$

where $\phi_0 = \theta_0 + \beta_0$, and $\phi_i = \theta_0 + \delta_i + \beta_i$. Furthermore, the geometric constraints between every wheel and the center of gravity of the vehicle are written as:

$$\left.\begin{aligned} x_1 &= x_0 + l_f \cos\theta_0 - d_L \sin\theta_0 \\ x_2 &= x_0 - l_r \cos\theta_0 - d_L \sin\theta_0 \\ x_3 &= x_0 - l_r \cos\theta_0 + d_R \sin\theta_0 \\ x_4 &= x_0 + l_f \cos\theta_0 + d_R \sin\theta_0 \end{aligned}\right\} \rightarrow x_i = x_0 + X_i \tag{19}$$

$$\left.\begin{array}{l} y_1 = y_0 + l_f \sin\theta_0 + d_L \cos\theta_0 \\ y_2 = y_0 - l_r \sin\theta_0 + d_L \cos\theta_0 \\ y_3 = y_0 - l_r \sin\theta_0 - d_R \cos\theta_0 \\ y_4 = y_0 + l_f \sin\theta_0 - d_R \cos\theta_0 \end{array}\right\} \rightarrow y_i = y_0 + Y_i \tag{20}$$

5.2.2 Steering maneuvers

To elaborate upon the desired steering angle of each wheel δ_{di}, first, by transforming the nonholonomic constraints, Equation (18), we obtain the following:

$$\delta_{di} = \tan^{-1}(\dot{y}_i/\dot{x}_i) - \theta_d - \beta_i \tag{21}$$

Subsequently, substituting Equations (19) and (20) into Equation (21), δ_{di} is derived by the following equation:

$$\delta_{di} = \tan^{-1}\left(\frac{v_d \sin\theta_d - \dot{Y}_i(\dot{\theta}_d)}{v_d \cos\theta_d - \dot{X}_i(\dot{\theta}_d)}\right) - \theta_d - \beta_i \tag{22}$$

where v_d represents the desired linear velocity of vehicle and $\dot{\theta}_d$ is the desired turning angular velocity of vehicle, which is calculated by Equations (15) and (16).

5.2.3 Driving maneuvers

The driving maneuver is achieved by the control of the wheel's angular velocity ω_i. The relationship between ω_i and wheel's linear velocity v_i can be written as:

$$\omega_i = v_i \cos\beta_i / r \tag{23}$$

Here, v_i can be expressed by $\dot{x}_i$ or $\dot{y}_i$:

$$v_i = \dot{x}_i / \cos\phi_i = \dot{y}_i / \sin\phi_i \tag{24}$$

Substituting Equation (19) or Equation (20) into the above equations, the desired angular velocity of the wheel ω_{di} can be obtained:

$$\omega_{di} = \begin{cases} (v_d \cos\theta_d + \dot{X}_i(\dot{\theta}_d))\cos\beta_i / r\cos\phi_i & (\theta_d \leq \pi/4) \\ (v_d \sin\theta_d + \dot{Y}_i(\dot{\theta}_d))\cos\beta_i / r\sin\phi_i & (\theta_d \geq \pi/4) \end{cases} \tag{25}$$

Additionally, ω_{di} has to be adjusted to compensate for the longitudinal wheel slippage measured as the slip ratio s_i. The improved desired angular velocity $\hat{\omega}_{di}$ compensating for the longitudinal slippage is rewritten as follows:

$$\hat{\omega}_{di} = \omega_{di} / (1 - (s_{ref} - s_i)) \tag{26}$$

where s_{ref} represents a reference slip ratio to regulate the longitudinal wheel slippage.

6 Slope Traversal Experiment with Sensor-based Feedback Control

In order to validate the proposed sensor-based feedback control, side-slope traversal experiments were carried out using our rover test bed on the test filed, as described in Section 4. The performance of the proposed control is evaluated on the basis of the distance and orientation errors.

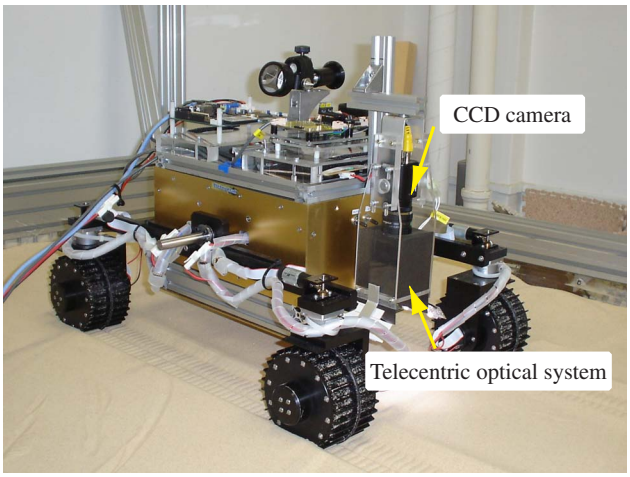

Figure 16: Rover test bed with visual odometry sensor

6.1 Measurement System for Vehicle

Measurements of the slip motions are the key procedure to achieve the proposed control. As defined in Equations (12), (13), and (14) the slip motion can be calculated by the velocities of the vehicle and wheel. As noted in Section 2, conventional odometry with a wheel encoder lacks sufficient accuracy of traveling velocity because of wheel slippage.

In this research, visual odometry using a CCD camera is employed for the position and velocity measurements. With this system, the traveling velocity of the vehicle is estimated by the optical flow vectors between the time consecutive images taken by a face down camera, which is mounted on the test bed and vertically looks at the terrain surface, as shown in Figure 16. In such a camera configuration, the size of the image varies according to the distance between the camera head and the target terrain, and then, accurate measurements of velocity are not achieved because the distance varies owing to the dynamic motion of the vehicle as well as the terrain roughness, as shown in Figure 17-a). Therefore, the scale factor needs to be multiplied in accordance with the distance in order to adequately measure the optical flows, but this requires an additional sensor to measure the distance between the camera head and the terrain surface.

In order to solve this problem, a telecentric lens is inserted in front of the camera head as shown in Figure 18. This lens realizes a *telecentric optical system* that provides a constant image scale factor regardless of the distance between the lens and the target. Figure 17-b) illustrates that the three images show the same size even though the distance of the object from the camera head varies from 30 [mm] to 130 [mm]. Therefore, the camera with the telecentric system guarantees sufficient accuracy in the optical flow calculation and velocity measurement of the vehicle without any additional measurement device or compensation for the scale factor. This visual odometry sensor using a telecentric system achieves the position measurement with 1.0 [mm] resolution and the travel distance within a few percentage points. The sampling rate of this sensor is 1/30 [sec].

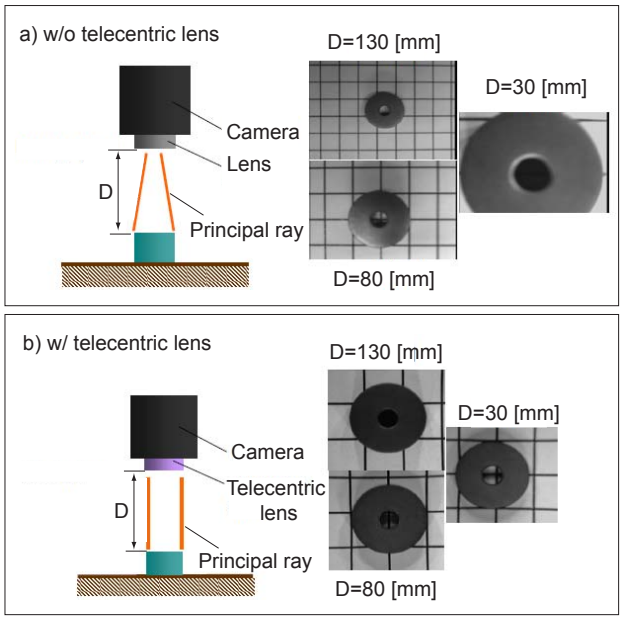

Figure 17: a) upper: Scale factor variances due to the camera height using conventional optics. b) lower: Scale factor invariance regardless of the camera height using the telecentric lens

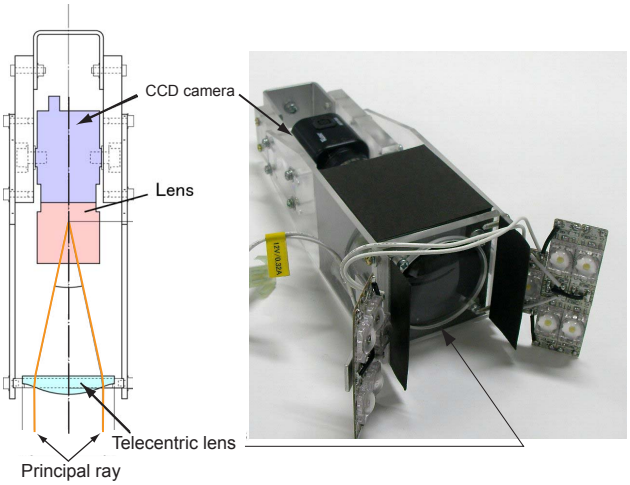

Figure 18: Visual odometry camera with telecentric lens

Table 5: Control gains for the sensor-based feedback control

k_1	k_2	k_3	k_4	k_5	k_6
100.0	2.0	0.2	0.05	2.0	0.2

The vehicle orientation for the roll and pitch axes are measured by two inclinometers fixed to each axis of the rover. The orientation around the yaw axis is calculated by integral of angular velocity data taken by a vibrating structure gyroscope mounted on the rover. These measurements for the orientation are conducted every 0.02 [sec].

6.2 Experimental Condition and Procedure

The set of experiments was conducted in two cases with varied slope angles of 5.0 [deg] (case-C) and 10 [deg] (case-D). The reference path to be followed was given as a straight path along with the side-slope traversal direction.

In the case of the control with slip compensation, the control variable for path following was distributed into the steering and driving axles on the front wheels, while the rear wheels work to compensate for the vehicle sideslip. The sensor-based feedback control was conducted every 0.2 [sec]. The desired velocity v_d is given as 0.02 [m/s], and the desired orientation θ_d as 0 [deg]. The control gains are summarized in Table 5. On the other hand, in case with no-control, every steering angle was fixed to maintain the angle of 0 [deg] and every wheel was controlled to maintain a constant velocity of 0.3 [rad/sec].

The experimental procedures are summarized as follows:

1. Set the rover test bed along with x axis of the slope coordinate (no initial heading error).
2. Measure the position, velocity, and orientation of the rover using the sensors mounted on the rover.
3. Calculate the distance and orientation errors, slip ratio and slip angle of every wheel, and the slip angle of the vehicle.
4. Determine the path following and slip compensation inputs on the basis of Equations (15) and (16).
5. Derive the steering and driving maneuvers by using Equations (22) and (26).
6. Input the calculated maneuvers to the steering and driving axles.
7. Return to step 2.

6.3 Experimental Resultsand Discussion

Figure 19 shows the snapshots when the rover traversed a slope of 10 [deg] with and without the slip compensation control. The experimental results for the slope traversal trajectory of

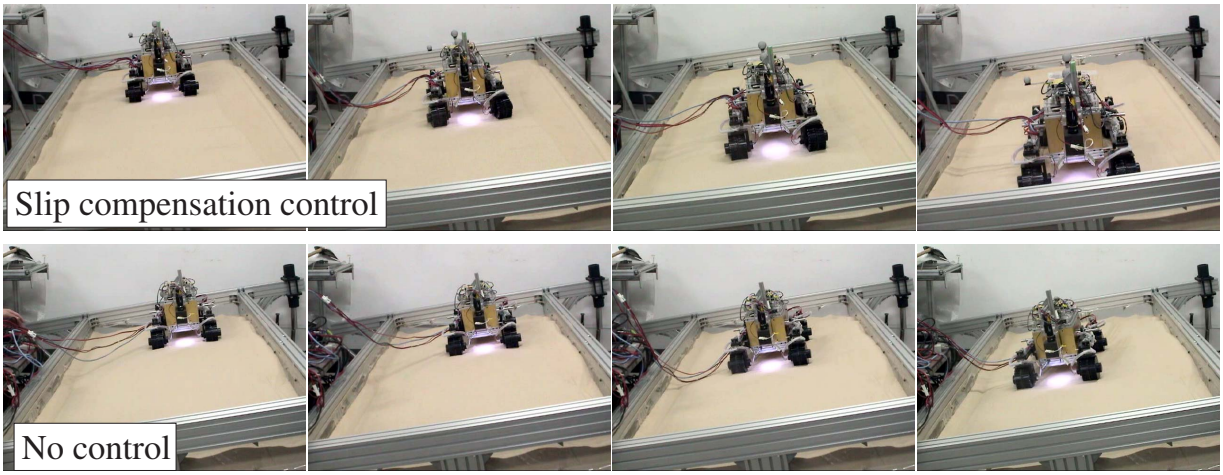

Figure 19: Snapshots of the slope traversal experiments, slope angle = 10 [deg] (above : Slip compensation control, below : No control)

Table 6: Path-following errors : Sensor-based feedback control

Slope anlge [deg]	Orientation error [deg]		Distance error [m]	
	rms	Final state	rms	Final state
Case-C 5.0 (#1)	1.94 (2.15 %)	2.72 (3.02 %)	0.003 (0.33 %)	0.001 (0.10 %)
(#2)	0.96 (1.06 %)	0.74 (0.83 %)	0.015 (1.34 %)	0.014 (1.28 %)
Case-D 10.0 (#1)	5.03 (5.59 %)	5.90 (6.55 %)	0.009 (0.84 %)	0.016 (1.53%)
(#2)	2.18 (2.42 %)	0.49 (0.55 %)	0.015 (1.20 %)	0.018 (1.43%)
Average	2.53 (2.81 %)	2.46 (2.74 %)	0.011 (1.05 %)	0.012 (1.23%)

the rover are shown in Figures 20 and 21. We have conducted certain number of test runs and this paper presents two typical experimental results in every case. In the graph, the red line with triangle markers indicates the trajectory obtained by the visual odometry in the case with the proposed control, the black line with circle markers is the ground truth of the trajectory measured by the stereo motion capture camera (detail of this camera is already described in Section 4), and the blue line with square markers shows the ground truth in the no-control case. Furthermore, errors in the distance and orientation are summarized in Table 6. The errors are evaluated by both the root mean square (rms) and the final state errors. The error percentage for the distance is calculated by dividing the error value by the length of the reference path, while that for the orientation is determined by dividing the error value by $\pi/2$.

From the results of the slope traversal trajectory, it can be clearly seen that the rover with the sensor-based feedback control can execute a straight-line traversal. In particular, it must be emphasized that the distance errors are in a negligible order, since each error value is almost equal to the sensor accuracy of the visual odometry system. The orientation errors are also controlled to be less than a few degrees.

In each experiment, the rear wheel pairs successfully compensate for the vehicle slip angle

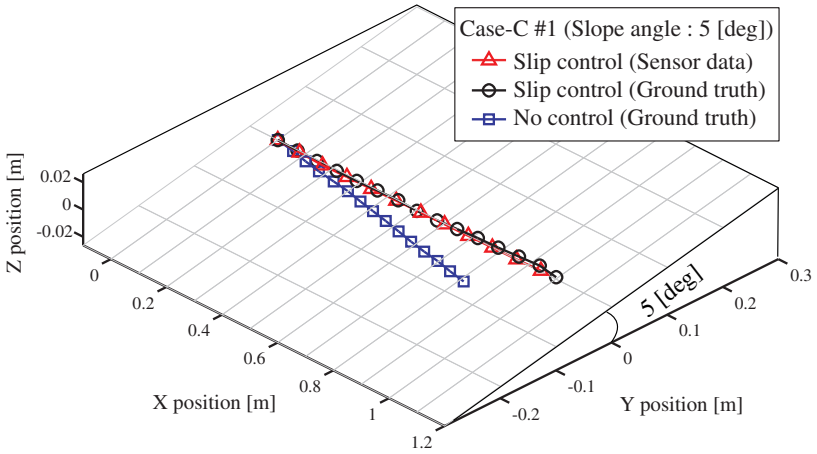

Case-C # 1

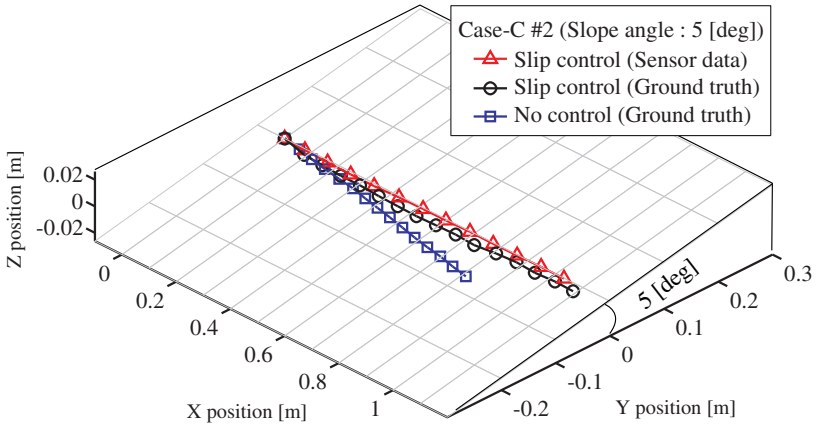

Case-C # 2

Figure 20: Slope traversal trajectory: case-C (Slope angle = 5.0 [deg])

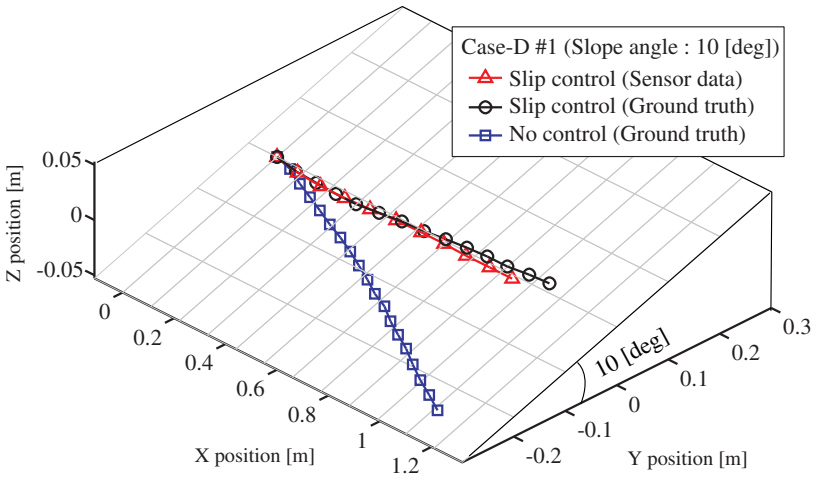

Case-D # 1

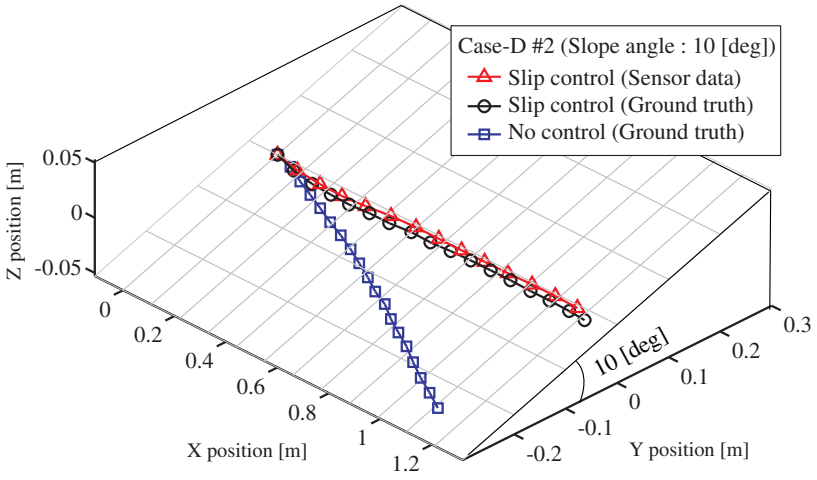

Case-D # 2

Figure 21: Slope traversal trajectory : case-D (Slope angle = 10.0 [deg])

within a few degrees. Subsequently, steering maneuvers compensates for the wheel slip angles and simultaneously follow a given path, even though the slip angles were approximately observed to be in the range of -10 [deg] to 20 [deg]. Furthermore, the wheel slip ratios can be significantly managed to be less than 0.4. From the results, the proposed control enables the rover to maneuver with appropriate counter-steering/driving motions, and the rover can then follow a straight path as well as compensate for dynamic slip motions even in the slope traversal situation on loose sand.

As observed in Table 6, the error percentage of orientation error is larger than that of the distance error. This is deduced due to an imperfect setting of the gains for orientation error. As defined in Equations (15) and (16), the proposed control consists of the P feedback control for the distance error and the PD feedback control for the orientation error. From the experiments, we could observe different motion behaviors with the different control gains. It is noteworthy that the controller gains in the experiment were given as fixed values for all cases for fair comparisons, but, for better performance they could be adjusted along with the slope angle, terrain characteristics, and the shape of the reference paths.

Compared to other conventional path-following methods or slip compensation controls, the advantages of the proposed sensor-based feedback method are summarized as follows: 1) vehicle sideslip and wheel longitudinal/lateral slips are completely included into the control maneuver, 2) controls for path following and slip compensation are respectively fulfilled by giving different control inputs to front/rear wheel pairs, and 3) the control approach can be utilized to any vehicles traveling on unknown terrain with varied types of soils.

7 Conclusions

In this paper, two different control schemes, the model-based feed-forward control and the sensor-based feedback control, have been proposed to enable exploration rovers to traverse on sandy-sloped terrain.

As for the model-based feed-forward control, we addressed the slope traversal criteria paying attention to the wheel forces and then developed the thrust-cornering characteristic diagram on the basis of the well-defined wheel force model. Three distinct traversal motions of the rover have been analytically clarified by illustrating the slope traversal criteria on the diagram. Furthermore, an appropriate steering maneuver for slope traversal can be determined by using the diagram

On the other hand, the sensor-based feedback control enables the rover to follow a path based on distance and orientation errors while simultaneously compensating dynamic slip motions. Three types of slip, namely, vehicle sideslip and longitudinal/lateral slips of the wheel, have been clearly discussed from the viewpoints of the nonholonomic constraints of the vehicle as well as the feedback control maneuvers. In particular, the tasks of path following and slip compensation have been achieved by distributing different control inputs to the front/rear wheel pairs,

The main contributions of this paper can be summarized in the following three points:

- Two different control schemes for a rover traversing sandy-sloped terrain have been proposed on the basis of the approaches of model-based/sensor-based and feed-forward/feedback controls.
- The thrust-cornering characteristic diagram has been developed to address the slope traversal. This diagram indicates slope traversal cases of the rover with quantitative slip conditions. The model-based steering maneuvers for slope traversal can be found using this diagram.
- Feedback control inputs sufficiently consider all vehicle/wheel slips. In addition, we have properly addressed the manner for deriving steering/driving maneuvers to realize the feedback control with taking the slippage into account.

Both control approaches have been validated through the slope traversal experiments. The effectiveness of the proposed control has been verified by quantitative evaluations of distance and orientation errors. From the experimental results, the distance error percentages of the sensor-based feedback control are less than 3.0 %, while those of the model-based feed-forward control are less than 7.5 %. In addition, the orientation error of both controls is less than 3.0 %. This confirms that the rover with the proposed controls could make appropriate steering and driving maneuvers to traverse the sandy-sloped terrain with sufficient accuracy as well as to reduce the sideslip of the rover even in a high-slip environment.

For further discussion, the comparison of the two proposed approaches is summarized as follows:

Model-based feed-forward control

Advantages: Initial errors that will occur in the feedback control can be compensated by this approach. The control system becomes much simpler than the feedback approach since this feed-forward scheme needs only low-level steering/driving control, which satisfies the feed-forward values. In addition, it should be noted that the thrust-cornering characteristic diagram is able to predict the traversability of the rover from the point of view of wheel-terrain interactions. This is useful to previously estimate large wheel slippages that will cause a vehicle to get stuck in loose sand.

Disadvantages: Modeling errors of the diagram due to the uncertainty of soil parameters make the performance worse. This approach requires accurate information in terms of terrain characteristics, including soil parameters, to calculate the diagram and to then determine the steering/driving maneuver.

Sensor-based feedback control

Advantages: This approach can be applied to any unknown terrain with varying types of soil and to any vehicle traveling in a slippery environment. In addition, we can apply this control to the arbitrary shapes of a reference path. Furthermore, the control scheme monitors the wheel slippage in every control loop so that the rover can avoid large wheel slippage while traversing on sloped terrain.

Disadvantages: A rover experiences a relatively large degree of error in the initial few centimeters because the control starts working only after the sensor system detects any errors in position or orientation. In addition, the error due to false measurements of sensors and insufficient tunings of the control gain would happen.

Based on the above discussion, each approach has conflicting disadvantages, which can be summarized as two concerns; one is model error and sensor error, and the other is feed-forward and feedback. One possible approach to compensate for these disadvantages is to incorporate the sensor-based control into the model-based control. The errors due to the modeling error can be compensated by the sensor-based feedback approach. In addition, the control-delay of the feedback can be solved by the feed-forward approach.

Acknowledgement

This work was performed at Tohoku University and partially supported Research Fellowships of the Japan Society for the Promotion of Science for Young Scientists.

References

Angelova, A., Matthies, L., Helmick, D., and Perona, P. (2007). Learning slip behavior using automatic mechanical supervision. In *Proceedings of the 2007 IEEE Int. Conf. on Robotics and Automation*, pages 1741–1748, Rome, Italy.

Angelova, A., Matthies, L., Helmick, D., Sibley, G., and Perona, P. (2006). Learning to predict slip for ground robots. In *Proceedings of the 2006 IEEE Int. Conf. on Robotics and Automation*, pages 3324–3331, Orlando, FL.

Bekker, M. G. (1960). *Off-the-Road Locomotion*. Ann Arbor, MI, USA, The University of Michigan Press.

Bekker, M. G. (1969). *Introduction to Terrain-Vehicle Systems*. Ann Arbor, MI, USA, The University of Michigan Press.

Coelho, P. and Nunes, U. (2005). Path-following control of mobile robots in presence of uncertainties. *IEEE Transactions on Robotics*, 21:252–261.

Gibbesch, A. and Schäfer, B. (2005). Multibody system modeling and simulation of planetary rover mobility on soft terrain. In *Proceedings of the 8th Int. Symp. on Artificial Intelligence, Robotics and Automation in Space (i-SAIRAS '05)*, Munich, Germany.

Helmick, D. M., Cheng, Y., Clouse, D. S., Matthies, L. H., and Roumeliotis, S. I. (2004). Path following using visual odometry for a mars rover in high-slip environments. In *Proceedings of the 2004 IEEE Aerospace Conference*, pages 772–789, Montana, MT.

Helmick, D. M., Roumeliotis, S. I., Cheng, Y., Clouse, D. S., Bajracharya, M., and Matthies, L. H. (2006). Slip-compensated path following for planetary exploration rovers. *Advanced Robotics*, 20:1257–1280.

Iagnemma, K. and Dubowsky, S. (2004). *Mobile Robots in Rough Terrain : Estimation, Motion Planning, and Control with Application to Planetary Rovers (Springer Tracts in Advanced Robotics)*, volume 12. Springer.

Iagnemma, K., Shibly, H., and Dubowsky, S. (2002). On-line traction parameter estimation for planetary rovers. In *Proceedings of the 2002 IEEE Int. Conf. on Robotics and Automation (ICRA2002)*, pages 3142–3147, Washington DC.

Ishigami, G., Miwa, A., Nagatani, K., and Yoshida, K. (2007). Terramechanics-based model for steering maneuver of planetary exploration rovers on loose soil. *Journal of Field Robotics*, 24:233–250.

Ishigami, G., Nagatani, K., and Yoshida, K. (2008a). Slope traversal experiments with slip compensation control for lunar/planetary exploration rover. In *Proceedings of the 2008 IEEE Int. Conf. on Robotics and Automation (ICRA2008)*, pages 2295–2300, Pasadena, CA.

Ishigami, G., Nagatani, K., and Yoshida, K. (2008b). Trafficability analysis for lunar/planetary exploration rover using thrust-cornering characteristic diagram. In *Proceedings of the 2008 IEEE Int. Conf. on Intelligent Robots and Systems (IROS2008)*, pages 2228–2233, Nice, France.

Jain, A., Guineau, J., Lim, C., Lincoln, W., Pomerantz, M., Sohl, G., and Steele, R. (2003). Roams: Planetary surface rover simulation environment. In *Proceedings of the 7th Int. Symp. on Artificial Intelligence, Robotics and Automation in Space (i-SAIRAS '03)*, Nara, Japan.

Kobayashi, T., Ochiai, H., Yasufuku, N., Omine, K., Aoki, S., Kanamori, H., Matsui, K., and Miyahara, A. (2006). Load-settlement characteristics of japanese lunar soil simulant in partial gravity. In *Preprints of Space Resources Roundtable VIII*, Golden, CO.

Lamon, P. (2005). *3D POSITION TRACKING FOR ALL-TERRAIN ROBOTS*. PhD thesis, EPFL, Lausanne.

Lamon, P. (2008). *3D-Position Tracking and Control for All-Terrain Robots (Springer Tracts in Advanced Robotics)*, volume 43.

Luca, A. D., Oriolo, G., and Samson, C. (1998). *Robot Motion Planning and Control*, chapter 4. Springer-Verlag.

Maimone, M., Cheng, Y., and Matthies, L. (2007). Two years of visual odometry on the mars exploration rovers. *Journal of Field Robotics*, 24:169–186.

Ojeda, L., Cruz, D., Reina, G., and Borenstein, J. (2006). Current-based slippage detection and odometry correction for moble robots and planetary rovers. *IEEE Transactions on Robotics*, 22:365–377.

Reina, G., Ojeda, L., Milella, A., and Borenstein, J. (2006). Wheel slippage and sinkage detection for planetary rovers. *IEEE/ASME Transactions on Mechatronics*, 11:185–195.

Rezaei, S., Guivant, J., and Nebot, E. M. (2003). Car-like robot path following in large unstructured environments. In *Proceedings of the 2003 IEEE Int. Conf. on Intelligent Robots and Systems (IROS2003)*, pages 2468–2473, LasVegas, NV.

Rio, F. D., Jimenez, G., Sevillano, J. L., Vicente, S., and Balcells., A. C. (1999). A generalization of path following for mobile robots. In *Proceedings of the 1999 IEEE Int. Conf. on Robotics and Automation (ICRA1999)*, pages 7–12, Detroit, MI.

Toyoura Sand (2008). Retrieved June 30, 2008, from http://www.toyourakeiseki.com/product-e.htm.

Wit, C. C., Khennouf, H., Samson, C., and Sordalen, O. J. (1994). *Recent Trends in Mobile Robots (World Scientific Series in Robotics and Automated Systems)*, volume 11, chapter 5. World Scientific Pub Co Inc.

Wong, J. Y. (2001). *Theory of Ground Vehicles, 3rd edition*. John Wiley & Sons.